Andreas Jäger[a], Roman Lackner[a,b], Klaus Stangl[c]
[a] Institute for Mechanics of Materials and Structures, Vienna University of Technology, Vienna, Austria
[b] Computational Mechanics, Technical University of Munich, Munich, Germany
[c] Institute for Road Construction and Maintenance, Vienna University of Technology, Vienna, Austria

Microscale characterization of bitumen – back-analysis of viscoelastic properties by means of nanoindentation

In order to understand the complex thermo-rheological behavior of asphalt, stemming from the viscoelastic nature of bitumen, the nanoindentation (NI) technique is employed. Hereby, the load history applied onto the indenter tip is characterized by a loading, holding, and unloading phase. As regards the identification of viscoelastic properties, a recently published back-analysis scheme, employing the holding phase of the NI test, is extended towards fractional-creep models. In fact, this type of model is found to perfectly describe the viscoelastic behavior of bitumen. Based on the identified viscoelastic model parameters, the influence of loading rate, maximum load, and temperature on these parameters is investigated. Hereby, the temperature dependence of creep parameters follows an Arrhenius-type law. In addition to the model parameters, application of the so-called grid-indentation technique within NI testing provides insight into the bitumen microstructure and the mechanical behavior of the different bitumen phases. The results obtained indicate the existence of a string-like microstructure embedded into a less viscous matrix material.

Keywords: Bitumen; Creep; Viscoelasticity; Nanoindentation

1. Introduction

Bitumen is the binder material of asphalt and determines its complex thermo-rheological behavior. For example, the low viscosity of asphalt at high temperatures ($T > 135\,^{\circ}\mathrm{C}$) is a necessary prerequisite for the construction and compaction process of high-quality asphalt layers. However, when the surface temperature reaches $70\,^{\circ}\mathrm{C}$ during hot summer periods, this viscosity should be significantly higher in order to minimize the development of permanent deformations in asphalt pavements (rutting). The desirable increase in viscosity and, hence, increase in stiffness from hot to medium temperatures ($0 < T < 70\,^{\circ}\mathrm{C}$) are, on the other hand, disadvantageous at low temperatures ($T < 0\,^{\circ}\mathrm{C}$), causing low-temperature cracking in asphalt pavements.

In general, the viscosity of bitumen can be described by a linear function in the log(viscosity)–temperature diagram (see Fig. 1). This relation may be optimized with respect to climate conditions and expected traffic load by the proper choice of the crude oil used in the bitumen production process and the so-called cut-point, defining the temperature during vacuum distillation. The goal of this optimization process is threefold:

1. Maintain low viscosities at high temperatures for construction and compaction;
2. Ensure high viscosity and elastic behavior at medium temperatures to avoid rutting; and
3. Ability of stress relaxation (sufficient small viscosity) at low temperatures.

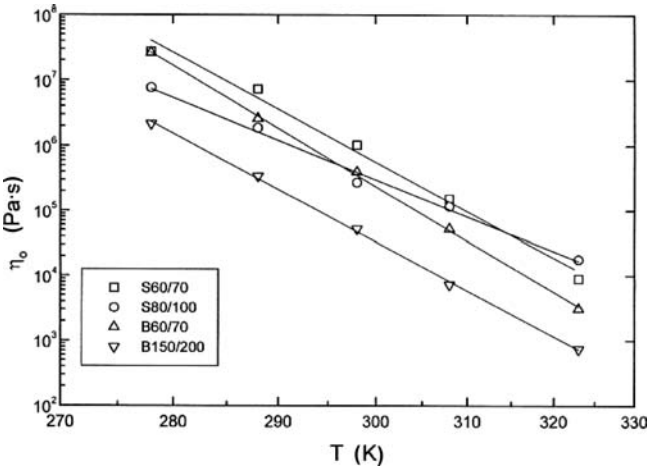

Fig. 1. Temperature dependence of the zero-shear-rate limiting viscosity for different types of bitumen [1].

In order to determine the origin of the viscoelastic behavior of bitumen, use of nanoindentation is proposed in this paper. In contrast to macroscopic tests, nanoindentation (NI) gives access to the mechanical properties and the microstructure at small length scales. In this paper, the mechanical properties obtained from NI testing are combined with chemical-test results and images from environmental scanning electron microscopy (ESEM), giving new insights into the complex thermo-rheological nature of bitumen.

2. Methods – nanoindentation

The main goal of NI is the identification of mechanical properties of the indented material. During NI measurements, a tip with defined shape penetrates the specimen surface with the indentation load P (N) and the penetration h (m) recorded as a function of time. Commonly, each indent

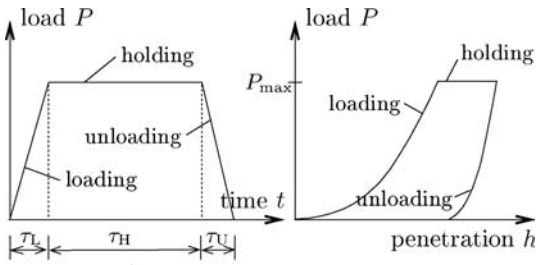

(a) (b)

Fig. 2. Illustration of (a) load history and (b) load–penetration curve of NI tests.

consists of a loading, holding, and unloading phase (see Fig. 2). During standard interpretation of NI test results, the hardness and the elastic material properties are determined:

- The hardness of the material, defined as $H = P_{\max}/A_c$ (Pa), is obtained from the loading phase of the NI test. Here, $P_{\max}$ (N) denotes the applied maximum load, and A_c (m^2) is the horizontal projection of the contact area at the end of the loading phase.
- According to [2, 3], the Young's modulus E of elastic or elastoplastic materials can be obtained from the relation between the measured initial slope of the unloading curve $S = dP/dh|_{h=h_{\max}}$ and the indentation modulus $M = E/(1-\nu^2)$, reading

$$S = \frac{2}{\sqrt{\pi}} M \sqrt{A_c} \tag{1}$$

where ν is Poisson's ratio, and A_c is the projected area of contact.

Parameter identification of materials exhibiting, in addition to elastic and plastic material response, time-dependent behavior (e. g., polymers, bitumen, etc.) requires back-analysis of the parameters from the holding phase of the measured penetration history $h(t)$. Recently, analytical solutions for the indentation of rigid tips into a viscoelastic halfspace were reported for spherical tips [4] and for perfect conical tips [5].

Since the shape of indenter tips varies as a consequence of the production process and in the course of testing due to attrition, the solution for the tip penetration, taking into account the real indenter shape, outlined in [6], is considered. Hereby, the geometrical representation of the indenter shape (with $A_{tip} = C_0 f(\rho)^2$ for perfect conical tips) is extended to

$$A_{tip} = \rho^2 \pi = C_0 f(\rho)^2 + C_1 f(\rho) \tag{2}$$

where A_{tip} (m^2) is the area of the cross section, and ρ (m) and $f(\rho)$ (m) are the corresponding radius and distance from the apex of the axisymmetric tip, respectively (see Fig. 3). C_0 (–) and C_1 (m) are constants describing the tip shape, which are generally provided during calibration of the NI equipment.

Based on the solution for the elastic indentation problem for the tip shape given in Eq. (2), the viscoelastic solution is obtained by the application of the method of functional equations [7] (see Appendix A). For the identification of viscoelastic model parameters of bitumen, this solution is specialized to two rheological models describing fractional creep: i. e., the nonlinear dash-pot (nlDP) and power-law (PL) creep model (see Fig. 4). The deviatoric creep compliance of both models reads

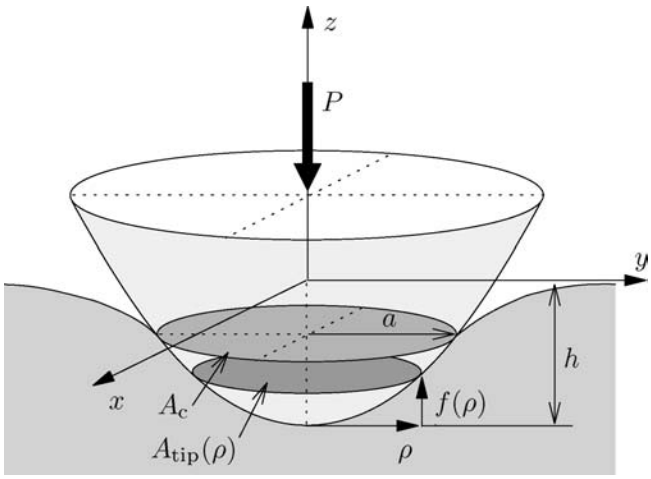

Fig. 3. Contact between a rigid axisymmetric indenter of shape $f(\rho)$ and an infinite halfspace (P is the applied load, h is the penetration, and a is the contact radius).

$$J_{nlDP} = J_a (t/\bar{\tau})^k \tag{3}$$

$$J_{PL} = J_0 + J_a (t/\bar{\tau})^k \tag{4}$$

where J_0 (GPa^{-1}) is the initial creep compliance describing the elastic behavior, J_a (GPa^{-1}) and k (–) characterize the time dependent behavior. $\bar{\tau}$ (s) is introduced for dimensional reasons and is set equal to 1 s.

In order to determine material parameters from NI test data, the error between the experimentally obtained function $F_{exp}(a)$ (depending on the contact radius a and determined from the penetration history $h(t)$ using Eqs. (10) and (12), see Appendix A) and the analytical result given in Eq. (28) is minimized within the holding period by adapting the unknown model parameters (see Fig. 5). For the case of the nlDP model, the error is defined by

$$R_{nlDP}(J_a, k) = \frac{e(J_a, k)}{u} \tag{5}$$

with

$$e^2(J_a, k) = \sum_{i=1}^{n} \left[F_{exp}\{a[h(t_i)]\} - F_{H-nlDP}(J_a, k, t_i)\right]^2 \tag{6}$$

and

$$u^2 = \sum_{i=1}^{n} F_{exp}^2(t_i) \tag{7}$$

where n is the number of selected time instants of the holding phase.

The error given in Eq. (5) is minimized by adapting the unknown model parameters J_a and k using a simplex iteration [8].

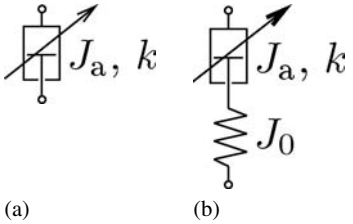

(a) (b)

Fig. 4. Creep models considered for back-analysis of viscoelastic parameters for bitumen: (a) Nonlinear dash-pot (nlDP) model and (b) power-law (PL) model.

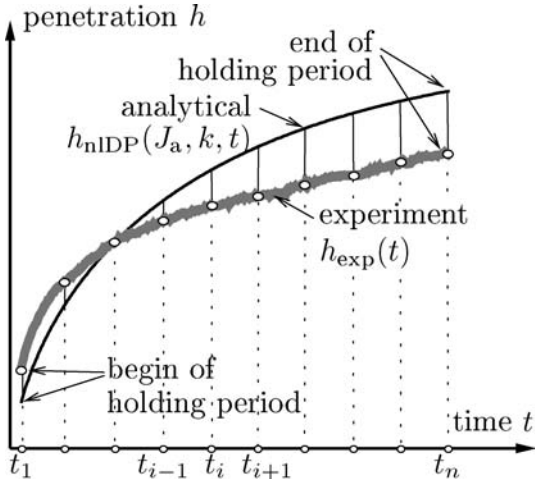

(a)

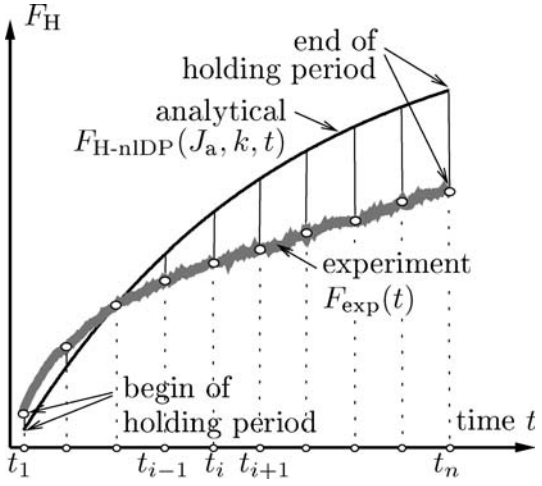

(b)

Fig. 5. Illustration of definition of the error used for parameter identification from the holding period of NI test data for the nlDP model: (a) Penetration history $h(t)$ and (b) evolution function F within the holding period.

3. Materials and experimental setup

Three types of bitumen, two plain bitumen (B50/70 and B50/70M4) and one polymer-modified bitumen (PmB60/90), are considered (the numbers indicate the range of penetration [9]). The polymer modified bitumen was obtained by the allowance of styrene-butadiene-styrene to the aforementioned B50/70M4. Additionally, aging of B50/70M4 and PmB60/90 was performed by means of the rolling-thin-film-oven test (RTFOT) according to [10] and, subsequently, by the pressure-aging vessel (PAV) according to [11]. The conventional properties of all three unaged bitumen (denoted as "A") and the RTFOT and PAV-aged bitumen (denoted as "C") are listed in Table 1. The result from elemental analysis is given in Table 2.

All NI tests were conducted using a Hysitron Triboindenter nanoindenter with a three-sided Berkovich diamond tip in a dry gas (nitrogen) environment, ensuring no water condensation on the sample surface for temperatures below the dew point. Calibration of the NI testing equipment revealed $C_0 = 24.5$ and $C_1 = 2314$ nm, describing the tip shape (see Eq. (2)).

Table 1. Conventional properties of types of bitumen considered (A: original bitumen, C: RTFOT + PAVaged) (parameters according to [9, 12, 13]).

Bitumen	Penetration point ($\frac{1}{10}$ mm)	Softening point (°C)	Fraaß breaking point (°C)
B50/70-A	49	50.5	−13
B50/70M4-A	54	48.8	−20
B50/70M4-C	27	64.8	–
PmB60/90-A	73	86.1	−28
PmB60/90-C	36	79.8	–

Table 2. Elemental composition (in mass%) of considered types of bitumen [14].

Bitumen	C	H	O	N	S	Σ
B50/70-A	83.0	10.4	–	1.1	5.1	99.6
B50/70M4-A	83.9	10.4	<0.1	0.4	5.0	99.7
B50/70M4-C	83.7	10.5	<0.1	0.5	4.9	99.6
PmB60/90-A	84.3	10.3	0.6	0.4	4.3	99.9
PmB60/90-C	84.0	10.2	0.9	0.5	4.4	100.0

4. Presentation of results and discussion

The presented parameter identification scheme was applied to the types of bitumen listed in Table 1. For each type of bitumen, grid indentation [15] characterized by 10×10 indents was performed. Figure 6 shows the frequency plots for J_a, k, and the error R_{nlDP} for B50/70-A tested at $-1\,^\circ$C. The values for the error R_{nlDP} are less than 3 %, confirming the proper choice of the nlDP model for representing the viscoelastic response of bitumen. The frequency plots obtained for J_a and k are approximated by a Gaussian distribution, giving mean values and standard deviations for the model parameters. For the considered type of bitumen (B50/70-A), the mean values of the model parameters corresponding to $T = -1\,^\circ$C are: $J_\mathrm{a} = 8.39\,\mathrm{GPa}^{-1}$ and $k = 0.71$. In the following, the mode of parameter identification outlined is employed to study

- the influence of the loading rate and the maximum load on the identified parameters,
- the temperature dependence of the model parameters, and
- the microstructure and the mechanical properties of the different bitumen phases.

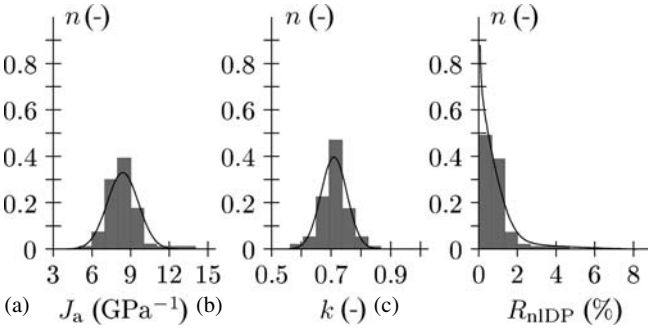

Fig. 6. Identification of model parameters for B50/70-A tested at $-1\,^\circ$C: Frequency plots for (a) J_a (GPa^{-1}), (b) k (–), and (c) error R_{nlDP} (%) (NI test conditions: $P_{\max} = 20$ µN, $\dot{P} = \mathrm{d}P/\mathrm{d}t = 40$ µNs^{-1}, $\tau_\mathrm{H} = 5$ s).

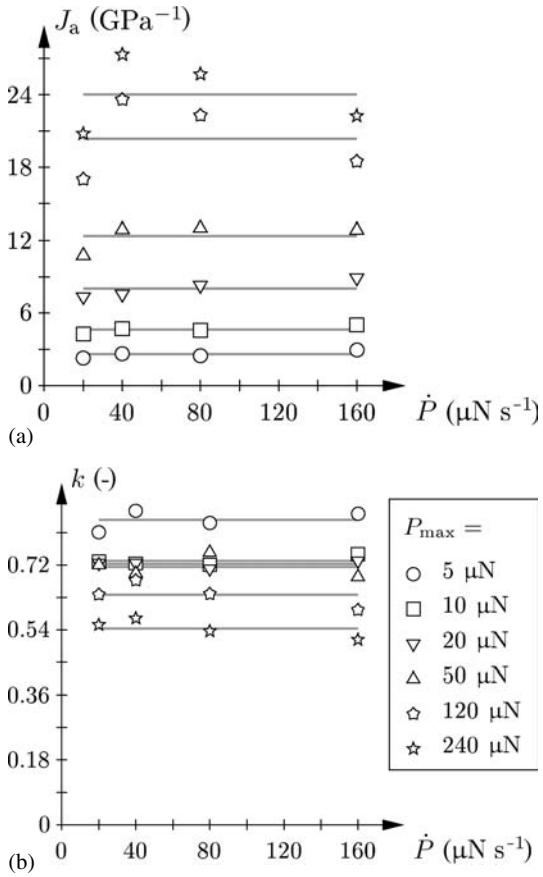

Fig. 7. Influence of loading rate and maximum load on nlDP model parameters: Mean value of (a) J_a [GPa^{-1}] and (b) k [−] [bitumen B50/70-A tested at $T = -1\,^{\circ}$C; $P_{max} = 5$, 10, 20, 50, 120, 240 μN; $\dot{P} = dP/dt = 20$, 40, 80, 160 μN s^{-1}; $\tau_H = 5$ s (for $P_{max} = 10$, 20 μN) and 10 s (for $P_{max} = 5$, 50, 120, 240 μN)].

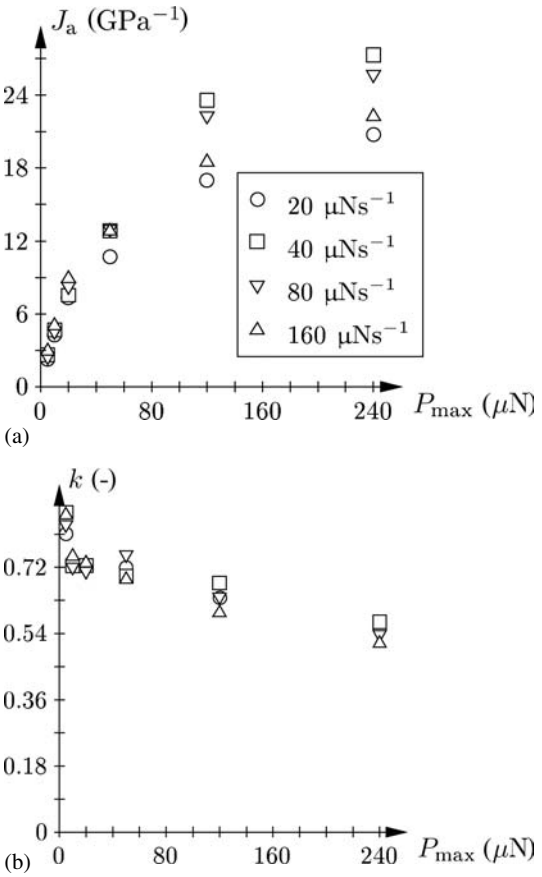

Fig. 8. Influence of maximum load on nlDP model parameters: Mean values for (a) J_a (GPa^{-1}) and (b) k (−) [bitumen B50/70-A tested at $T = -1\,^{\circ}$C; $P_{max} = 5$, 10, 20, 50, 120, 240 μN; $\dot{P} = dP/dt = 20$, 40, 80, 160 μN s^{-1}; $\tau_H = 5$ s (for $P_{max} = 10$, 20 μN) and 10 s (for $P_{max} = 5$, 50, 120, 240 μN)].

4.1. Influence of loading rate and maximum load

Figure 7 shows the mean values of the nlDP model parameters for different loading rates and different values for the maximum load obtained from grid indentations on bitumen B50/70-A at $-1\,^{\circ}$C (with $\dot{P} = dP/dt = 20$, 40, 80, 160 μN s^{-1} and $P_{max} = 5$, 10, 20, 50, 120, 240 μN). Whereas the influence of the loading rate on the parameters is quite small for all considered load levels, the maximum load itself has a high impact on the obtained model parameters (see Fig. 8). By increasing the maximum load, J_a increases until it seems to reach a limiting value. The parameter k, on the other hand, decreases almost continuously with increasing maximum load (see Fig. 8b). The variation of the identified model parameters with the maximum load and, consequently, with the penetration depth is explained by the bitumen microstructure, consisting of viscous strings embedded into a low-viscous matrix (see Subsection 4.3).

The back-analysis scheme itself provides a unique solution during identification of J_a–k pairs corresponding to the different maximum loads. The identified J_a–k pairs corresponding to different maximum loads were used in the analytical solution for the penetration history given in Fig. 9. As the maximum load used for parameter identification increases, the variation in the penetration histories decreases, indicating the decreased influence of the bitumen microstructure as the penetration depths during parameter identification increase.

4.2. Temperature dependence of model parameters

Accounting for the thermo-rheological behavior of bitumen, the influence of the temperature on model parameters is studied by conducting NI tests at different temperatures. Figures 10a and b show mean values of the nlDP model

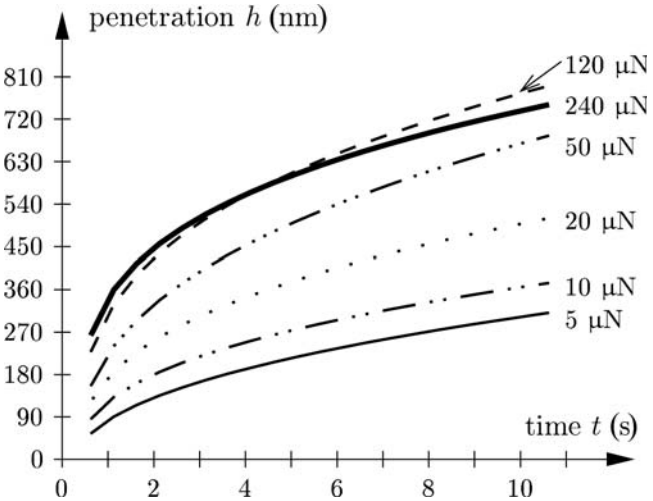

Fig. 9. Analytical solution for penetration history $h(t)$ for $P_{max} = 50$ μN, $\dot{P} = 80$ μN s^{-1}, $\tau_H = 10$ s) (given values refer to maximum load used in NI tests for parameter identification, leading to different J_a–k pairs).

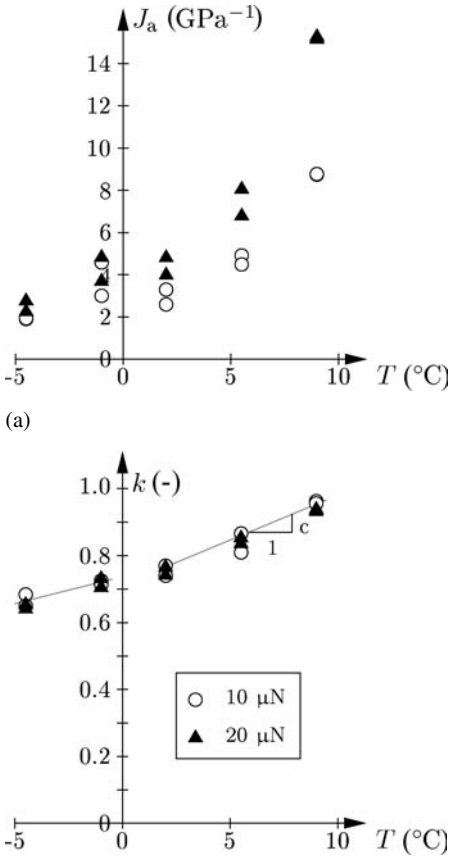

Fig. 10. Temperature dependence of nlDP model parameters for bitumen B50/70-A: Mean values for (a) J_a (GPa^{-1}) and (b) k (–) (NI test conditions: P_{max} = 10, 20 µN, $\dot{P}$ = dP/dt = 20, 40 µN s^{-1}, τ_H = 10 s).

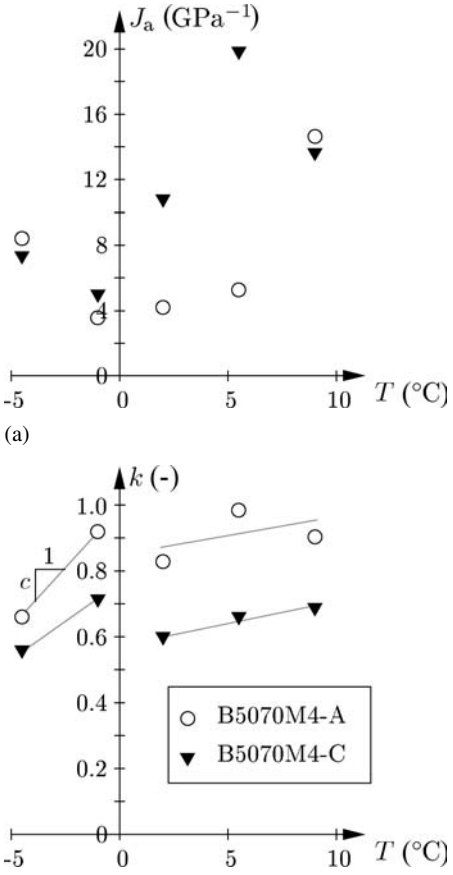

Fig. 11. Temperature dependence of nlDP model parameters for bitumen B50/70M4-A/-C: Mean values for (a) J_a (GPa^{-1}) and (b) k (–) (NI test conditions: P_{max} = 10 µN, $\dot{P}$ = dP/dt = 20 µN s^{-1}, τ_H = 10 s).

parameters for bitumen B50/70-A tested at $T = -4.5$; -1; 2; 5.5; 9 °C. Whereas J_a increases from -4.5 to -1 °C, slightly decreases from -1 to 2 °C, and finally increases again from 2 to 9 °C, the parameter k increases continuously with increasing temperature. The temperature dependence of the parameter k is approximated by two lines, with the slope of the lines being different for temperatures below -1 °C and for temperatures above 2 °C (see Table 3). The increase of both J_a and k indicate the expected increase in the creep compliance with increasing temperature. The change of the parameters between -1 and 2 °C might be related to chemo-physical processes, observed during testing of bitumen by means of modulated differential scanning calorimetry, where an exothermic peak was found for B50/70-A at this temperature range [16].

Figures 11 and 12 show mean values of the nlDP model parameters for the bitumen B50/70M4 and PmB60/90M4 (A- and C-aged) tested at $T = -4.5$; -1; 2; 5.5; 9 °C. As regards J_a, a decrease from -4.5 to -1 °C, followed by an increase from -1 to 9 °C was observed for both types of bitumen and aging states. The parameter k, on the other hand, increases from -4.5 to -1 °C, slightly decreases from -1 to 2 °C, and finally increases again from 2 to 9 °C (for the values of c, see Table 3). As for the bitumen B50/70-A, the change of J_a between -4.5 and -1 °C and the change of k between -1 and 2 °C is assigned to changes in the molecular structure observed by means of modulated differential scanning calorimetry.

The temperature dependence of J_a depicted in Figs. 13 and 14 is well-described by an Arrhenius-type law in the temperature regime outside the aforementioned re-arrangement of molecules, reading:

$$J_a = \bar{J}_a(\bar{T}) \exp\left[-\frac{E_a}{R}\left(\frac{1}{T} - \frac{1}{\bar{T}}\right)\right] \tag{8}$$

where $\bar{T}$ (K) is the reference temperature, R is the gas constant, and E_a (J mol^{-1}) is the activation energy. The ratio of the activation energy and the gas constant, E_a/R, is given in Table 3 for all types of bitumen considered. Interestingly, the activation energy for bitumen B50/70-A computed for the whole tested temperature range (dashed line in Fig. 13), with $E_a/R = 8500$ K, agrees very well with the value obtained from macroscopic bending-beam-rhe-

Table 3. Ratio of the activation energy and the gas constant E_a/R, and slope c describing the temperature dependence of k for considered types of bitumen.

Bitumen	E_a/R (K)	c (–4.5 to –1 °C) (K^{-1})	c (2 to 9 °C) (K^{-1})
B50/70-A	13 000	0.018	0.028
B50/70M4-A	10 300	0.074	0.011
B50/70M4-C	6700	0.044	0.013
PmB60/90-A	12 500	0.055	0.003
PmB60/90-C	5400	0.041	0.007

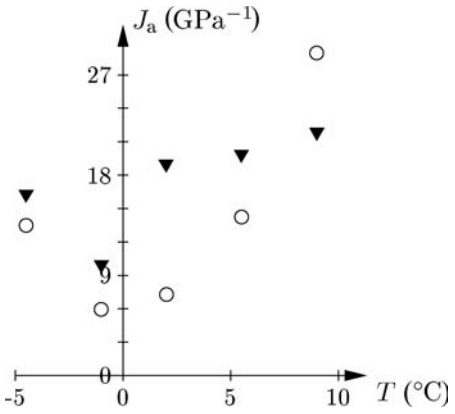

(a)

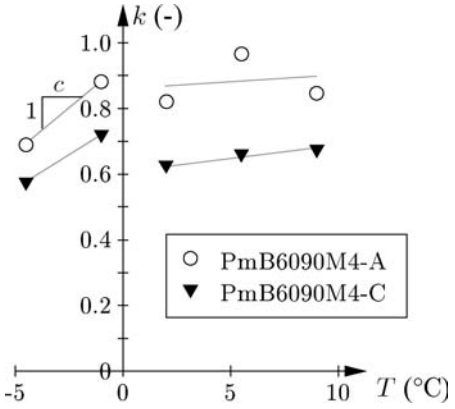

(b)

Fig. 12. Temperature dependence of nlDP model parameters for bitumen PmB60/90M4-A/-C: Mean values for (a) J_a (GPa^{-1}) and (b) k (–) (NI test conditions: P_{max} = 10 μN, $\dot{P}$ = dP/dt = 20 μN s^{-1}, τ_H = 10 s).

ometer tests of bitumen, revealing a value of E_a/R of 9000 K [17].

Finally, the values for J_a and k obtained for bitumen B50/70-A were compared with the results obtained from standard bitumen tests, such as the bending beam rheometer (BBR) and the dynamic shear rheometer (DSR) operating in different temperature regimes. Figure 15 shows good agreement between the obtained parameters from NI and the respective standard test data. The NI data obtained fit well into the larger temperature range covered by the standard test methods (–24 to 40 °C).

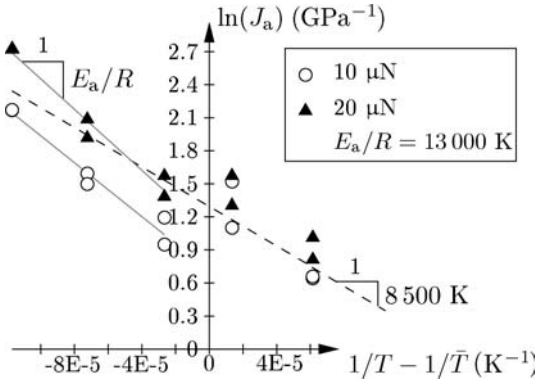

Fig. 13. Identification of Arrhenius-type law describing the temperature dependence of J_a (GPa^{-1}) for bitumen B50/70-A ($\bar{T}$ = 273 K).

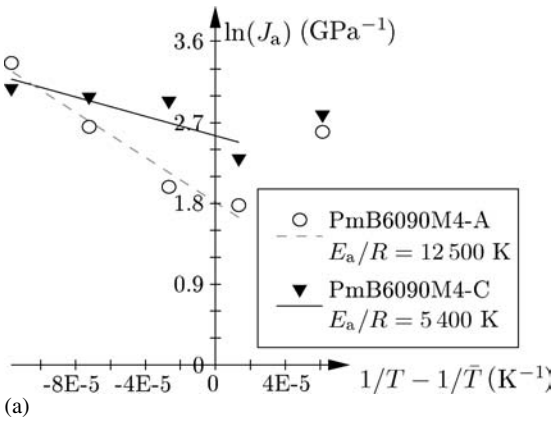

(a)

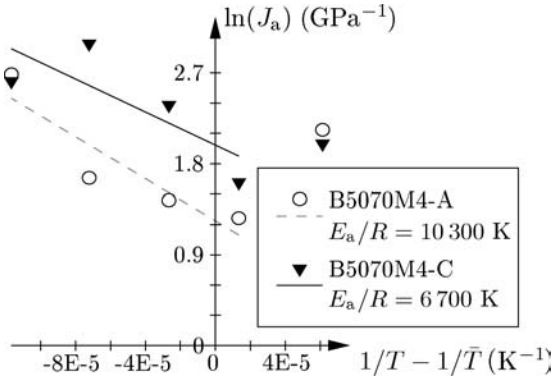

(b)

Fig. 14. Identification of Arrhenius-type law describing the temperature dependence of J_a (GPa^{-1}) for bitumen B50/70M4-A/-C and PmB60/90M4-A/-C ($\bar{T}$ = 273 K).

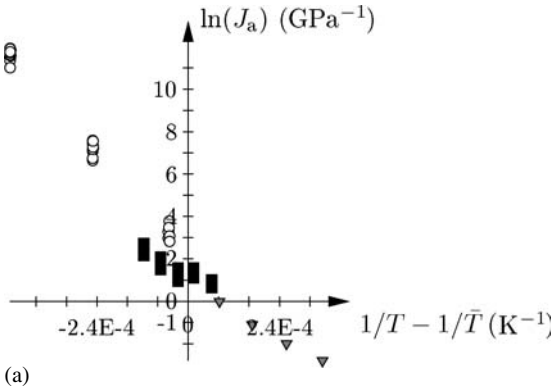

(a)

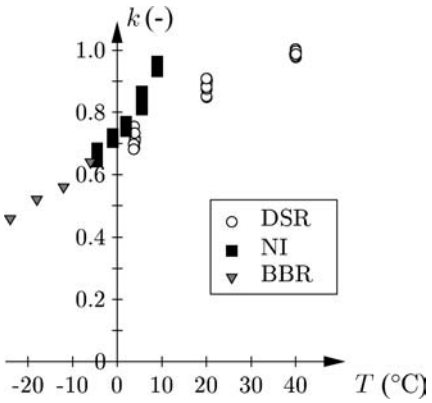

(b)

Fig. 15. Comparison of model parameters (a) J_a (GPa^{-1}) and (b) k (–) obtained from NI testing with DSR and BBR data for bitumen B50/70-A ($\bar{T}$ = 273 K).

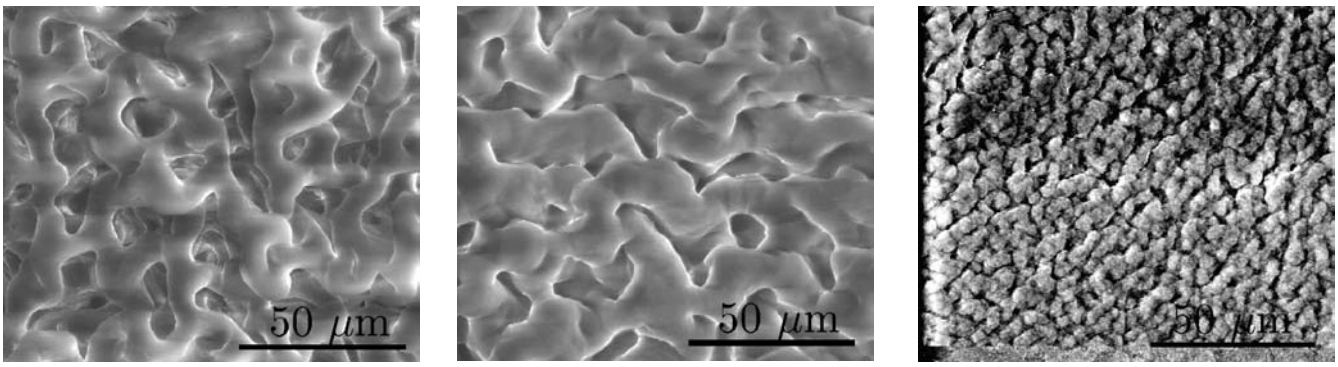

(a) (b) (c)

Fig. 16. Environmental scanning electron microscopy (ESEM) images of (a) unaged, (b) RTFOT-aged, and (c) RTFOT + PAV-aged bitumen B50/70 [21].

4.3. Bitumen treated as a multiphase composite

Bitumen is the remaining part during crude-oil distillation and, hence, its chemical composition strongly depends on the origin of the crude oil. Its main constituents are hydrocarbons with different amounts of polarity, and a molecular mass ranging from 300 to 100 000 g mol^{-1} [18, 19]. This complex chemical composition results in an arrangement within the molecular cocktail in bitumen, characterized by a string-like structure embedded in a matrix substance [20]. Interestingly, the string-like structures change their properties with aging (see Fig. 16) [21] and they align under external loading [20].

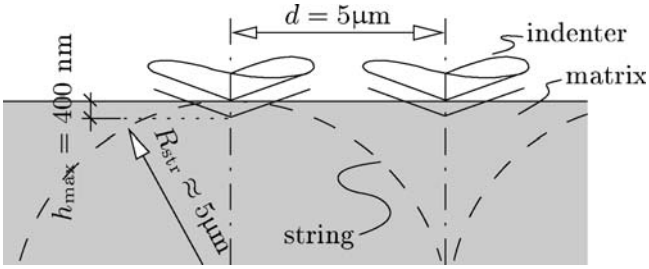

Fig. 17. Determination of appropriate distance between adjacent grid points from (i) bitumen microstructure and (ii) the maximum penetration depth.

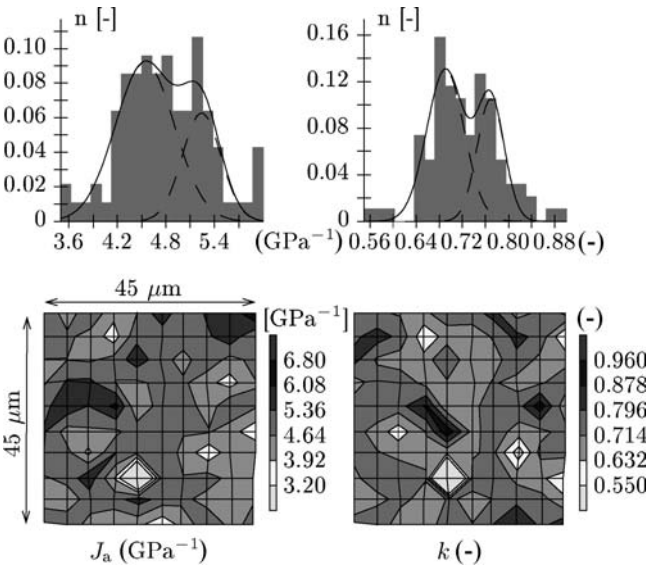

Fig. 18. Frequency plot and corresponding grid plot for parameters of nlDP model: (a) J_a (GPa^{-1}) and (b) k (–) (bitumen B50/70-A tested at $T = -1$ °C, $P_{max} = 10$ μN, $\tau_L = 0.25$ s, $\tau_H = 5$ s).

In order to identify the mechanical properties of the two bitumen phases, the grid indentation technique [15] is employed. With the characteristic dimension of the bitumen microstructure of 10 μm (diameter of strings according to [21]), the distance between adjacent grid points is set to 5 μm. Using a Berkovich tip for the indentation experiments, the distance between adjacent indents of 5 μm gives a maximum penetration of 400 nm, ensuring no interaction between two adjacent indents (see Fig. 17).

Figure 18 shows frequency plots and the corresponding grid plots for the parameters of the nlDP model obtained from grid indentation on B50/70-A tested at –1 °C. The grid plots confirm the microstructure already observed by ESEM [20, 21], showing a string like microstructure with typical dimensions of about 10 μm embedded into a matrix material. The histograms emphasize the presence of two bitumen phases exhibiting different mechanical behavior. Whereas the strings show lower values of J_a and k, higher values for the matrix are observed. The approximation of the frequency plots by two Gaussian distributions gives the mean values and the standard deviation of the model parameters for the two bitumen phases.

5. Concluding remarks

The identification of viscoelastic properties of bitumen and its material phases by means of nanoindentation was presented in this paper. The back-analysis scheme proposed in [6] was extended towards implementation of two fractional creep models, i.e., the nonlinear dash-pot and the power-law model. In order to identify the material parameters of bitumen and to validate the performance of the proposed analysis scheme, NI tests on different types of bitumen were performed for different loading rates, maximum loads, and at different temperatures. The parameters for the nlDP model were determined from the holding period of the penetration histories. Based on the so-obtained parameters, the following conclusions can be drawn:

1. The increase in the maximum load resulted in a significant variation of the model parameters. This effect was attributed to the microstructure of bitumen present at the scale of NI testing.

2. The loading rate, on the other hand, showed marginal influence on the parameters, reflecting the ability of the parameter identification scheme presented to capture time-dependent material behavior.
3. The temperature dependence of the parameter J_a was successfully described by an Arrhenius-type law. The change in the bitumen microstructure, observed earlier by means of modulated differential scanning microscopy, was reflected by a variation of the model parameters in the respective temperature regime.
4. The model parameters obtained from NI testing fit well into results from standard test methods.
5. The results from grid indentation gave insight into the microstructure of bitumen showing the string-like structure already observed by environmental scanning electron microscopy. Hereby, the strings were described by lower values of the viscoelastic model parameters, whereas higher values for the matrix were observed.

The nonlinear dash-pot (nlDP) model employed for parameter identification gave excellent agreement between the experimentally-obtained NI penetration curves and the model response. According to bending-beam-rheometer tests the nlDP model is able to capture both the short- as well as the long-term response of bitumen.

The authors thank the remaining members of the Christian Doppler Laboratory for 'Performance-Based Optimization of Flexible Pavements' at Vienna University of Technology for helpful comments and fruitful discussions on the presented research work. Financial support by the Christian Doppler Gesellschaft (Vienna, Austria) is gratefully acknowledged.

A. Analytical solution for viscoelastic indentation problem – specialization for power-law model

A.1. Elastic indentation problem

For the solution of the elastic indentation problem, i.e., a rigid indenter penetrating the elastic halfspace (see Fig. 3), the so-called Sneddon solution [2] is employed and specialized for the function $f(\rho)$ describing the tip shape, with

$$f(\rho) = \frac{1}{2C_0}\left(\sqrt{C_1^2 + 4C_0\rho^2\pi} - C_1\right) \tag{9}$$

Here, ρ (m) is the radius of the axisymmetric tip, and C_0 (–) and C_1 (m) are constants describing the tip shape. According to [6], the penetration h (m) and the corresponding load P (N) are related through the contact radius a,

$$h = a\sqrt{\frac{\pi}{C_0}}\arctan\frac{2a\sqrt{C_0\pi}}{C_1} \tag{10}$$

$$P = 4\pi\frac{E}{1-\nu^2}\frac{2a^3}{3C_1}{}_2F_1\left(1/2;2;5/2;-\frac{4a^2C_0\pi}{C_1^2}\right) = MF(a) \tag{11}$$

where M is the indentation modulus, with $M = E/(1-\nu^2)$, and $F(a)$ is a function depending only on geometric properties, such as the tip shape (described by C_0 and C_1) and the contact radius a, reading

$$F(a) = 4\pi\frac{2a^3}{3C_1}{}_2F_1\left(1/2;2;5/2;-\frac{4a^2C_0\pi}{C_1^2}\right) \tag{12}$$

In Eqs. (11) and (12), ${}_2F_1(a;b;c;z)$ denotes a hypergeometric function, defined as (see, e.g., [26])

$${}_2F_1(a;b;c;z) = \frac{\Gamma(c)}{\Gamma(b)\Gamma(c-b)}\int_0^1 \frac{t^{b-1}(1-t)^{c-b-1}}{(1-tz)^a}\mathrm{d}t \tag{13}$$

A.2. Viscoelastic indentation problem – consideration of trapezoidal load history

The elastic indentation problem outlined in the previous subsection is extended to linear viscoelasticity by the method of functional equations [7]. Following the method of functional equations, the viscoelastic solution for the indentation problem is obtained from the elastic solution by replacing the elastic operators P, M, and $F(a)$ in Eq. (11) by their Laplace transforms $\widehat{P(s)}$, $\widehat{M(s)}$, and $\widehat{F(a(s))}$, giving

$$\widehat{P(s)} = \widehat{M(s)}\;\widehat{F(a(s))} \tag{14}$$

Re-arrangement yields an expression for the Laplace transform of the function $F(a(s))$ as

$$\widehat{F(a(s))} = \frac{\widehat{P(s)}}{\widehat{M(s)}} = \frac{1}{s\widehat{M(s)}}s\widehat{P(s)} = \widehat{\bar{Y}(s)}\;s\widehat{P(s)} \tag{15}$$

where $1/(s\widehat{M(s)})$ was replaced by the Laplace transform of $\bar{Y}(t)$, in the following referred to as the indentation compliance function. Considering that (i) a multiplication by s in the Laplace domain is equivalent to a derivation in the time domain and (ii) a multiplication of two Laplace-transformed functions is equivalent to the convolution product of the two functions in the time domain, $F(t)$ is obtained from Eq. (15) as

$$F(t) = \int_0^t \bar{Y}(t-\tau)\frac{\mathrm{d}P(\tau)}{\mathrm{d}\tau}\mathrm{d}\tau \tag{16}$$

with $P(t)$ representing the load hist ory.

Since indentation tests are commonly conducted under load control, Eq. (16) is specified to the trapezoidal load history depicted in Fig. 2a, reading

$$P(t) = \begin{cases} P_L(t) = t/\tau_L P_{max} & \text{for} \quad 0 \le t \le \tau_L \\ P_H(t) = P_{max} & \text{for} \quad \tau_L \le t \le \tau_L + \tau_H \\ P_U(t) = (\tau_L + \tau_H + \tau_U - t)/\tau_U P_{max} & \\ \text{for} \quad \tau_L + \tau_H \le t \le \tau_L + \tau_H + \tau_U & \end{cases} \tag{17}$$

where τ_L, τ_H, and τ_U are the loading, holding, and unloading durations, respectively. Considering the load history $P(t)$ given in Eq. (17) in Eq. (16), the function $F(t)$ becomes for the loading and holding regime

$$F_L(t) = \int_0^t \bar{Y}(t-\tau)\frac{\mathrm{d}}{\mathrm{d}\tau}P_L(\tau)\,\mathrm{d}\tau = \frac{P_{max}}{\tau_L}\int_0^t \bar{Y}(t-\tau)\,\mathrm{d}\tau \tag{18}$$

$$F_H(t) = \int_0^{\tau_L} \bar{Y}(t-\tau)\frac{\mathrm{d}}{d\tau}P_L(\tau)\,\mathrm{d}\tau + \int_{\tau_L}^t \bar{Y}(t-\tau)\frac{\mathrm{d}}{\mathrm{d}\tau}P_H(\tau)\,\mathrm{d}\tau$$

$$= \frac{P_{max}}{\tau_L}\int_0^{\tau_L} \bar{Y}(t-\tau)\,\mathrm{d}\tau \tag{19}$$

Based on F_L and F_H in Eqs. (18) and (19), the history of the penetration, $h(t)$, for the loading and holding time is determined in three steps:

1. First, the indentation compliance function $\bar{Y}(t)$ appearing in Eqs. (18) and (19) is determined for the viscoelastic model considered. In the case of elastic material response, the indentation modulus M can be expressed by the bulk modulus K and the shear modulus μ_0, reading

$$M = \frac{E}{1-\nu^2} = \frac{\dfrac{9K\mu_0}{3K+\mu_0}}{1-\left(\dfrac{3K-2\mu_0}{6K+2\mu_0}\right)^2} = 4\mu_0\frac{3K+\mu_0}{3K+4\mu_0} \quad (20)$$

In order to determine material parameters for bitumen from NI test data, the indentation modulus M (see Eq. (20)) is specialized for incompressible materials, with $K=\infty$, giving

$$M = 4\mu_0 \quad (21)$$

Applying the method of functional equations [7], the elastic constant μ_0 in Eq. (21) is replaced by the associated Laplace transformed operator $\widehat{\mu(s)}$, reading

$$\widehat{M(s)} = 4\widehat{\mu(s)} \quad (22)$$

For the power-law (PL) model $\widehat{\mu(s)}$ is obtained as (see, e. g., [27]):

$$\widehat{\mu_{PL}(s)} = (s\mathcal{L}\{J_{PL}\})^{-1} = \left(s\mathcal{L}\left\{J_0 + J_a\left(\frac{t}{\bar{\tau}}\right)^k\right\}\right)^{-1} = \left(J_0 + J_a\frac{1}{s^k\,\bar{\tau}^k}\Gamma(1+k)\right)^{-1} \quad (23)$$

where $\mathcal{L}\{\bullet(t)\}$ denotes the Laplace transformation of $\bullet(t)$. Considering $\widehat{M(s)}$ of the PL model given in Eqs. (22) and (23) and applying the inverse Laplace transformation to $\widehat{\bar{Y}(s)} = 1/(s\widehat{M(s)})$, the indentation compliance function $\bar{Y}(t)$ is obtained as

$$\bar{Y}_{PL}(t) = \frac{1}{4}\left(J_0 + J_a\left(\frac{t}{\bar{\tau}}\right)^k\right) = \frac{1}{4}J_{PL} \quad (24)$$

2. Secondly, considering the indentation compliance function $\bar{Y}(t)$ for the PL model (Eq. (24)) in Eqs. (18) and (19), the function $F(t)$ is obtained for the loading and holding regime, $F_L(t)$ and $F_H(t)$, as

$$F_{L\text{-}PL}(t) = \frac{P_{max}}{\tau_L}\int_0^t \bar{Y}(t-\tau)\,\mathrm{d}\tau = \frac{P_{max}}{4\tau_L}\left\{J_0 t + J_a\frac{1}{(k+1)}\left(\frac{1}{\bar{\tau}}\right)^k t^{k+1}\right\} \quad (25)$$

$$F_{H\text{-}PL}(t) = \frac{P_{max}}{\tau_L}\int_0^{\tau_L} \bar{Y}(t-\tau)\,\mathrm{d}\tau = \frac{P_{max}}{4\tau_L}\left\{J_0\tau_L + J_a\frac{1}{(k+1)}\left(\frac{1}{\bar{\tau}}\right)^k \times \left[t^{k+1} - (t-\tau_L)^{k-1}\right]\right\} \quad (26)$$

Taking into account that the nlDP model is obtained from the PL model by setting J_0 equal to zero, $F_{L\text{-nlDP}}(t)$ and $F_{H\text{-nlDP}}(t)$ are obtained as

$$F_{L\text{-nlDP}}(t) = \frac{P_{max}}{4\tau_L}\left\{J_a\frac{1}{(k+1)}\left(\frac{1}{\bar{\tau}}\right)^k t^{k+1}\right\} \quad (27)$$

$$F_{H\text{-nlDP}}(t) = \frac{P_{max}}{4\tau_L}\left\{J_a\frac{1}{(k+1)}\left(\frac{1}{\bar{\tau}}\right)^k \left[t^{k+1} - (t-\tau_L)^{k+1}\right]\right\} \quad (28)$$

3. Finally, the history of the contact radius, $a(t)$, is obtained from combining the expressions for $F_L(t)$ and $F_H(t)$ given in Eqs. (25) to (28) with Eq. (12). The so-obtained (nonlinear) expression for $a(t)$ is solved numerically. With $a(t)$ at hand, the history of the penetration, $h(t)$, is given by Eq. (10) for a given load history $P(t)$ and the material model describing the behavior of the viscoelastic halfspace.

References

[1] P. Partal: Fuel 78 (1999) 1.
[2] I.N. Sneddon: Int. J. Eng. Sci. 3 (1965) 47.
[3] W.C. Oliver, G.M. Pharr: J. Mater. Res. 7 (1992) 1564.
[4] L. Cheng, X. Xia, L.E. Scriven, W.W. Gerberich: Mech. Mater. 37 (2005) 213.
[5] M. Vandamme, F.-J. Ulm: Int. J. Sol. Struct. 43 (2006) 3142.
[6] A. Jäger, R. Lackner, J. Eberhardsteiner: Meccanica (2007), in press.
[7] E.H. Lee, J.R.M. Radok: J. Appl. Mech. (1960) 438.
[8] W.H. Press, S.A. Teukolsky, W.T. Vetterling, B.P. Flannery: Numerical recipes in Fortran 77: The art of scientific computing, Vol. 1 of Fortran Numerical Recipes, Cambridge University Press, Cambridge (1996).
[9] ÖNORM EN 1426: Bitumen und bitumenhaltige Bindemittel – Bestimmmung der Nadelpenetration [Bitumen and bituminous binders – Determination of needle penetration], Österreichisches Normungsinstitut, Vienna (2000), in German.
[10] EN 12607-1: Bitumen and bituminous binders – Determination of the resistance to hardening under the influence of heat and air – Part 1: RTFOT method, European Committee for Standardization, Brussels (1999).
[11] prEN 14769: Bitumen and bituminous binders – Accelerated long-term ageing – Pressure ageing vessel (PAV), European Committee for Standardization, Brussels (2003).
[12] ÖNORM EN 1427: Bitumen und bitumenhaltige Bindemittel – Bestimmmung des Erweichungspunktes – Ring- und Kugel-Verfahren [Bitumen and bituminous binders – Determination of softening point – Ring and Ball method], Österreichisches Normungsinstitut, Vienna (2000), in German.
[13] ÖNORM EN 12593: Bitumen und bitumenhaltige Bindemittel – Bestimmmung des Brechpunktes nach Fraaß [Bitumen and bituminous binders – Determination of the Fraass breaking point], Österreichisches Normungsinstitut, Vienna (2000), in German.
[14] ASTM D5291: Standard test method for instrumental determination of carbon, hydrogen and nitrogen in petroleum products and lubricants, ASTM International, West Conshohocken (2002).
[15] G. Constantinides, K.S. Ravi Chandran, F.-J. Ulm, K.J. Van Vliet: Mater. Sci. Eng. A 430 (2006) 189.
[16] A. Jäger: Microstructural identification of bitumen by means of atomic force microscopy (AFM), modulated differential scanning calorimetry (MDSC), and reflected light microscopy (RLM), Master's Thesis, University of Technology, Vienna (2004).

[17] R. Lackner, M. Spiegl, R. Blab, J. Eberhardsteiner: J. Mater. Civ. Eng. (ASCE) 17 (2005) 485.
[18] Shell-Bitumen-U.K.: The Shell bitumen handbook, Vol. 1, Shell Bitumen UK, Chertsey (1990).
[19] G.D. Hobson: Modern petroleum technology, Part II, Vol. 5, The Institute of Petroleum, London (1984).
[20] S.J. Rozeveld, E.E. Shin, A. Bhurke, L. France, L.T. Drzal: Microscopy Res. Technique 38 (1997) 529.
[21] K. Stangl, A. Jäger, R. Lackner: Int. J. Road Mater. Pavement Design 7 (2006) 111.
[22] M. Abramowitz, I.A. Stegun: Handbook of mathematical functions, with formulas, graphs, and mathematical tables, Dover, New York (1972).
[23] W.N. Findley, J.S. Lai, K. Onaran: Creep and relaxation of nonlinear viscoelastic materials, Dover, New York (1989).

(Received October 11, 2006; accepted January 13, 2007)

Correspondence address

Andreas Jäger
Institute for Mechanics of Materials and Structures
Vienna University of Technology
Karlsplatz 13/202, A-1040 Vienna, Austria
Tel.: +43 1 58801 20218
Fax: +43 1 58801 20299
E-mail: Andreas.Jaeger@tuwien.ac.at